



HAL
open science

Observation of quantum de-trapping and transport of heavy defects in tungsten

Kazuto Arakawa, Mihai-Cosmin Marinica, Steven Fitzgerald, Laurent Proville, Duc Nguyen-Manh, Sergei Dudarev, Pui-Wai Ma, T D Swinburne, Alexandra Goryaeva, Tetsuya Yamada, et al.

► **To cite this version:**

Kazuto Arakawa, Mihai-Cosmin Marinica, Steven Fitzgerald, Laurent Proville, Duc Nguyen-Manh, et al.. Observation of quantum de-trapping and transport of heavy defects in tungsten. *Nature Materials*, 2020, 19, pp.508. 10.1038/s41563-019-0584-0 . hal-02457181

HAL Id: hal-02457181

<https://hal.science/hal-02457181>

Submitted on 17 Nov 2023

HAL is a multi-disciplinary open access archive for the deposit and dissemination of scientific research documents, whether they are published or not. The documents may come from teaching and research institutions in France or abroad, or from public or private research centers.

L'archive ouverte pluridisciplinaire **HAL**, est destinée au dépôt et à la diffusion de documents scientifiques de niveau recherche, publiés ou non, émanant des établissements d'enseignement et de recherche français ou étrangers, des laboratoires publics ou privés.

1 **Observation of quantum de-trapping and transport of heavy defects in tungsten**

2 Kazuto Arakawa^{1*}, Mihai-Cosmin Marinica², Steven Fitzgerald³, Laurent Proville²,
3 Duc Nguyen-Manh⁴, Sergei L. Dudarev⁴, Pui-Wai Ma⁴, Thomas D. Swinburne⁵,
4 Alexandra M. Goryaeva², Tetsuya Yamada⁶, Takafumi Amino⁷, Shigeo Arai⁸, Yuta
5 Yamamoto⁸, Kimitaka Higuchi⁸, Nobuo Tanaka⁸, Hidehiro Yasuda⁹, Tetsuya Yasuda⁹,
6 Hirotaro Mori⁹

7 ¹*Next Generation TATARA Co-Creation Centre, Organization for Industrial Innovation,*
8 *Shimane University, 1060 Nishikawatsu, Matsue 690-8504, Japan.*

9 ²*DEN-Service de Recherches de Métallurgie Physique, CEA, Université Paris-Saclay,*
10 *F-91191, Gif-sur-Yvette, France.*

11 ³*Department of Applied Mathematics, University of Leeds, Leeds LS2 9JT, UK*

12 ⁴*CCFE, United Kingdom Atomic Energy Authority, Culham Science Centre,*
13 *Oxfordshire OX14 3DB, United Kingdom.*

14 ⁵*CINaM-Aix Marseille Université-CNRS, 13009 Marseille, France.*

15 ⁶*Railway, Automotive & Machinery Parts Unit Osaka Steel Works, Nippon Steel &*
16 *Sumitomo Metal Corporation, 1-109, Shimaya 5-chome, Konohana-ku, Osaka 554-*
17 *0024, Japan.*

18 ⁷*Advanced Technology Research Laboratories, Nippon Steel & Sumitomo Metal*
19 *Corporation, 1-8 Fuso-Cho, Amagasaki, Hyogo 660-0891, Japan.*

20 ⁸*Institute of Materials and Systems for Sustainability, Nagoya University, Nagoya 464-*
21 *8603, Japan.*

22 ⁹*Research Centre for Ultra-High Voltage Electron Microscopy, Osaka University, 7-1*
23 *Mihogaoka, Ibaraki, Osaka 567-0047, Japan.*

24 *email: arakawa@riko.shimane-u.ac.jp

25

26 The diffusion of defects in crystalline materials¹ controls macroscopic behaviour in a
27 wide range of processes, including alloying, precipitation, phase transformation, and
28 creep². In real materials, intrinsic defects are unavoidably bound to static trapping
29 centres such as impurity atoms, meaning that their diffusion is dominated by de-
30 trapping processes. It is generally held that de-trapping occurs only by thermal
31 activation. In this Letter we report the first direct observation of the quantum de-
32 trapping of defects below around 1/3 of the Debye temperature. We successfully
33 monitored the de-trapping and migration of self-interstitial atom clusters, strongly
34 trapped by impurity atoms in tungsten, by triggering de-trapping out of equilibrium at
35 cryogenic temperatures, using high-energy electron irradiation and in-situ transmission
36 electron microscopy. The quantum-assisted de-trapping leads to low-temperature
37 diffusion rates orders of magnitude higher than a naive classical estimate suggests. Our
38 analysis shows that this phenomenon is generic to any crystalline material.

39

40

41 Under high-energy irradiation (or extreme mechanical deformation), atoms in a crystal
42 can be displaced significantly from their lattice positions, forming vacancy and self-
43 interstitial atom (SIA) defects. These are ultimately responsible for severe degradation
44 of the mechanical properties of materials, such as hardening, swelling, and
45 embrittlement³. Understanding the basic mechanisms controlling the formation and
46 diffusion of defects⁴⁻⁶ is critical for the development of future next-generation energy
47 systems.

48

49 In the field of material science, to the best of our knowledge, all the observed migration
50 processes of species heavier than H or He^{7,8} have been interpreted as resulting from

51 thermal activation characterized by the Arrhenius rate⁹, or phonon dragging^{10,11}. No
52 apparent quantum effects have been detected¹², although they have been theoretically
53 considered for SIAs¹³⁻¹⁵ and screw dislocations¹⁶. Quantum effects have also been
54 observed on metal surfaces¹⁷. We focus here on the low temperature diffusion of SIA
55 clusters in tungsten as a model for crystal defects in heavy-atom systems.

56

57 The lowest-energy SIA configuration in tungsten (and other non-magnetic body-
58 centred-cubic (bcc) transition metals) is a $\langle 111 \rangle$ crowdion, in which atomic
59 displacements are confined almost entirely to a $\langle 111 \rangle$ string containing an extra atom.
60 The defect is delocalized: it involves many more than one atom, as the displacement
61 field is spread down the string, resulting in very low barriers to translation (known as
62 *Peierls* barriers, see [Supplementary Discussion 1a](#) and [Fig. ED1](#)). Hence crowdions
63 perform one-dimensional (1D) diffusion along their axis with a low (meV scale)
64 activation energy^{10,18,19}. Similarly to single crowdions, SIA clusters in the form of $\mathbf{b} =$
65 $\frac{1}{2}\langle 111 \rangle$ dislocation loops undergo 1D glide diffusion in the direction of the Burgers'
66 vector \mathbf{b} . This phenomenon has been studied using classical molecular dynamics
67 simulations (MD)²⁰⁻²⁴ and transmission electron microscopy (TEM)^{5,25} for α -iron and
68 other metals and alloys.

69

70 According to MD studies, the activation energy (Peierls barrier) for cluster diffusion is
71 less than 0.1 eV^{20,22}, meaning they are thermally mobile even at very low temperatures.
72 In any real material however, impurity atoms (mainly carbon and nitrogen) act as traps
73 by binding to the clusters. Vacancies (expected at high density under irradiation) will
74 mutually annihilate with SIAs at the cluster boundary.

75

76 Previous studies, using resistivity recovery and internal friction experiments⁹, have
77 shown that low-temperature cluster migration in tungsten (and other bcc metals) is
78 strongly influenced by the concentration of impurity atoms²⁶⁻²⁸.

79

80 These traps are deep enough (~ 1 eV, see [Supplementary Discussion 1b](#) and [Fig. ED2](#))
81 to prevent TEM observation of the clusters' thermal escape and subsequent motion on
82 experimental timescales, even at 300 K, and they remain immobile. To overcome this,
83 we used the electron beam in transmission electron microscopes such as a high-voltage
84 electron microscope (HVEM) to enhance the vacancy mobility and reduce the effective
85 trap depth. In the absence of the electron beam, vacancies are immobile up to 620-
86 900K⁹, but in our experiment, the momentum imparted by the incident electrons moves
87 the vacancies up to 100 times per second. The experimental system is shown
88 schematically in [Fig. 1](#), and operates as follows.

89

90 First, a high energy (2000 keV) electron beam is used to create displacement damage,
91 vacancies and SIAs at 105 K, before aging at 300 K. This allows the SIA clusters to
92 nucleate and grow to nanoscale, with impurities bound to their perimeters (where the
93 binding energy is greatest). At these temperatures, the vacancies are thermally
94 immobile and remain dispersed throughout the sample. A lower energy (100-1000 keV)
95 electron beam is then turned on to illuminate the sample. The energy of incident
96 electrons is too low to create additional vacancies and SIAs, but high enough to
97 athermally move the existing vacancies (see [Methods](#)). Under the beam, the previously
98 trapped clusters begin to move ([Fig. 1](#); [Supplementary Video 1](#)). The principal quantity
99 we monitor is the cluster motion frequency. The precise definition of this quantity,
100 together with its dependence on the experimental irradiation conditions, is given in

101 [Methods](#) and illustrated in [Fig. 2](#). Perhaps the most striking feature of our study is the
102 possibility to resolve the SIA clusters' thermal and quantum-mechanical motion, even
103 in the presence of a flux of vacancies. In [Methods](#) we describe in detail how this is
104 achieved.

105 The key features of the observed motion of SIA clusters are:

- 106 i) hops are rare events, i.e. the clusters spend far more time being trapped than
107 travelling between traps;
- 108 ii) clusters sometimes move back and forth between fixed points in the sample;
- 109 iii) clusters are observed to shrink under the beam;
- 110 iv) motion frequency depends strongly on temperature.

111

112 i) and ii) tell us that the clusters are escaping from the impurity traps, moving quickly
113 through the lattice before being subsequently trapped again; iii) tells us how this occurs:
114 the radiation-mobilized vacancies move through the crystal, attracted to the areas of
115 highly compressive strain at the cluster boundaries. Here they annihilate with the SIAs
116 at the cluster boundaries, reducing the size of the cluster, and increasing the separation
117 between the impurity atom and the cluster boundary. The impurity-cluster interaction
118 is strong but short-ranged (see [Supplementary Discussion 1b](#) and [Fig. ED2](#)), and rapidly
119 vanishes over only a few lattice spacings, so that the traps are now much shallower, and
120 making cluster escape easier ([Fig. 2abc](#)). We now turn to the temperature dependence,
121 iv), which demonstrates that the low temperature escapes are quantum mechanical in
122 nature. It is noted that, for this purpose, we set the experimental system so that the
123 cluster escape processes by the direct electron collision with a cluster itself²⁹ or the
124 impurity that traps the cluster³⁰ can be neglected ([Methods](#)).

125

126 [Figure 3](#) is an Arrhenius plot showing the logarithm of the motion frequency vs. inverse
127 temperature. Hops due to thermal escape from potential wells of depth $\Delta V \gg k_B T$ have

128 a characteristic rate $\propto \exp(-\Delta V/k_B T)$, corresponding to a straight line on an Arrhenius
129 plot. This appears to be the case at higher temperatures $T \geq 50$ K and the slope suggests
130 that ΔV is higher than 10 meV. As temperature is reduced, $17 \text{ K} \leq T \leq 50 \text{ K}$, the slope
131 flattens as the de-trapping mechanism changes from classical thermal escape to
132 temperature-independent quantum mechanical diffusion.

133

134 The measured rates result from three independent processes: the athermal radiation-
135 driven vacancy migration under the beam (rate Γ_{vac}), the fluctuation-driven escape of
136 the cluster from the trap (depth ΔV_{trap} , rate Γ_{trap}), and finally the traversal of the Peierls
137 barrier intrinsic to the crystal (depth ΔV_p , rate Γ_p) (see [Methods](#)).

138

139 [Figure 3a](#) shows attempted classical fits for all barriers
140 $10 \text{ meV} \leq \Delta V = \Delta V_p + \Delta V_{\text{trap}} \leq 90 \text{ meV}$. Note that the Peierls traversal rate is non-
141 Arrhenius (since ΔV_p is not more than $k_B T$, see [Methods](#)), but no possible classical
142 form for the rate can explain the observed values. (We are able to state with confidence
143 that the sample temperatures continue to decrease below 50 K, and are not significantly
144 affected by beam heating – see [Supplementary Discussion 2 and Fig. ED3](#)).

145

146 In [Fig. 3b](#), we use a quantum mechanical form for the escape rate Γ^{QM} , derived from
147 the quantized nature of the crystal phonons (see [Methods](#)). These obey the Bose-
148 Einstein rather than the Boltzmann statistics, and their zero-point fluctuations increase
149 the average energy available for the cluster to overcome the barrier, thus increasing the
150 low temperature rates, in excellent agreement with experimental observations.
151 Moreover, the same quantum rates simultaneously fit two independent datasets,

152 acquired at two different electron accelerating voltages. This proves that the same
153 fundamentally quantum mechanism explains both datasets.

154

155 We are able to obtain acceptable fits for all barriers between 10 and 90 meV. To narrow
156 this down, we consider the critical temperature τ_c below which classical physics breaks
157 down (see [Methods](#)). This depends on the barrier height: [Figure 2](#) shows that the 90
158 meV fit clearly failing below 140 K, whereas the 10 meV one appears reasonable down
159 to around 50 K. τ_c depends on the phonon density of states, and is estimated³¹ to be 101
160 K for pure tungsten (about 1/3 of the Debye temperature). Fitted values for τ_c are also
161 shown in [Fig. 3](#), and the value of 101 K is consistent with a barrier height of 30 – 44
162 meV. We note that the resistivity recovery and internal friction experiments correspond
163 to the barrier height of 15 – 60 meV^{9,26-28}.

164

165 Other manifestations of quantum behaviour are in principle possible, in particular the
166 deep tunneling of the entire cluster. However, fitting the data to this functional form
167 requires unrealistic values for the cluster's effective mass (see [Methods](#)), and we
168 conclude that, over the range of temperatures probed by our experiments, quantized
169 phonons facilitating the clusters' escape from traps that are 30 – 44 meV deep provide
170 the optimal explanation of the data.

171

172

173 In this study we have performed the first direct investigation of cryogenic defect
174 diffusion using in-situ TEM. Our unique experimental system allowed us to manipulate
175 the effective potential wells encountered by SIA clusters, reducing their depth until we
176 could probe the quantum mechanical nature of their de-trapping. The quantum transport

177 becomes dominant below around $1/3$ of the Debye temperature. Moreover, the observed
178 behaviour derives from quantized phonons, which drive the stochastic fluctuations of
179 objects that are themselves too heavy to tunnel significantly. This likely affects the low
180 temperature transport of defects in many crystalline materials. Our results also
181 demonstrate the importance of quantum effects for low temperature defect evolution
182 even in heavy atom systems.

183 **References**

- 184 1 Mehrer, H. *Diffusion in Solids*. Vol. 155 (Springer, 2007).
 185 2 Gupta, D. *Diffusion Processes in Advanced Technological Materials*.
 186 (William Andrew Inc., 2005).
 187 3 Gary, S. W. *Fundamentals of Radiation Materials Science*. (Springer, 2007).
 188 4 Fu, C.-C., Torre, J. D., Willaime, F., Bocquet, J.-L. & Barbu, A. Multiscale
 189 modelling of defect kinetics in irradiated iron. *Nature Materials* **4**, 68-74
 190 (2005).
 191 5 Arakawa, K. *et al.* Observation of the one-dimensional diffusion of
 192 nanometer-sized dislocation loops. *Science* **318**, 956-959,
 193 doi:10.1126/science.1145386 (2007).
 194 6 Bai, X.-M., Voter, A. F., Hoagland, R. G., Nastasi, M. & Uberuaga, B. P.
 195 Efficient Annealing of Radiation Damage Near Grain Boundaries via
 196 Interstitial Emission. *Science* **327**, 1631-1634, doi:10.1126/science.1183723
 197 (2010).
 198 7 Kadono, R. *et al.* Quantum diffusion of positive muons in copper. *Physical*
 199 *Review B* **39**, 23-41 (1989).
 200 8 Sundell, P. G. & Wahnström, G. Activation energies for quantum diffusion of
 201 hydrogen in metals and on metal surfaces using delocalized nuclei within the
 202 density-functional theory. *Physical Review Letters* **92**, 155901 (2004).
 203 9 Ehrhart, P., Jung, P., Schultz, H. & Ullmaier, H. *Atomic Defects in Metals*.
 204 Vol. 25 (Springer-Verlag, Berlin, 1991).
 205 10 Derlet, P. M., Nguyen-Manh, D. & Dudarev, S. L. Multiscale modeling of
 206 crowdion and vacancy defects in body-centered-cubic transition metals.
 207 *Physical Review B* **76**, 054107 (2007).
 208 11 Swinburne, T. D., Dudarev, S. L. & Sutton, A. P. Classical Mobility of Highly
 209 Mobile Crystal Defects. *Physical Review Letters* **113**, 215501 (2014).
 210 12 Wollenberger, H. J. in *Physical Metallurgy, Part II* (eds R. W. Chan & P.
 211 Haasen) 1139 (North Holland Physics Publishing, Amsterdam, 1983).
 212 13 Pushkarov, D. I. Quantum theory of crowdions at low temperatures. *Soviet*
 213 *Journal of Experimental and Theoretical Physics* **37** (1973).
 214 14 Flynn, C. P. Resonance mode hopping and the stage I annealing of metals.
 215 *Thin Solid Films* **25**, 37-43, doi:http://dx.doi.org/10.1016/0040-
 216 6090(75)90242-4 (1975).
 217 15 Swinburne, T. D., Ma, P.-W. & Dudarev, S. L. Low temperature diffusivity of
 218 self-interstitial defects in tungsten. *New Journal of Physics* **19**, 073024 (2017).
 219 16 Proville, L., Rodney, D. & Marinica, M.-C. Quantum effect on thermally
 220 activated glide of dislocations. *Nat Mater* **11**, 845-849,
 221 doi:http://www.nature.com/nmat/journal/v11/n10/abs/nmat3401.html#supple
 222 mentary-information (2012).
 223 17 Ohresser, P. *et al.* Surface Diffusion of Cr Adatoms on Au(111) by Quantum
 224 Tunneling. *Physical Review Letters* **95**, 195901 (2005).
 225 18 Fitzgerald, S. P. & Nguyen-Manh, D. Peierls potential for crowdions in the
 226 bcc transition metals. *Physical Review Letters* **101**, 115504 (2008).
 227 19 Amino, T., Arakawa, K. & Mori, H. Detection of one-dimensional migration
 228 of single self-interstitial atoms in tungsten using high-voltage electron
 229 microscopy. *Sci Rep* **6**, 26099, doi:10.1038/srep26099 (2016).

- 230 20 Wirth, B. D., Odette, G. R., Maroudas, D. & Lucas, G. E. Dislocation loop
 231 structure, energy and mobility of self-interstitial atom clusters in bcc iron. *J*
 232 *Nucl Mater* **276**, 33-40, doi:http://dx.doi.org/10.1016/S0022-3115(99)00166-
 233 X (2000).
- 234 21 Marian, J. *et al.* Dynamics of self-interstitial cluster migration in pure α -Fe
 235 and Fe-Cu alloys. *Physical Review B* **65**, 144102 (2002).
- 236 22 Osetsky, Y. N., Bacon, D. J., Serra, A., Singh, B. N. & Golubov, S. I. One-
 237 dimensional atomic transport by clusters of self-interstitial atoms in iron and
 238 copper. *Philos Mag* **83**, 61-91, doi:10.1080/0141861021000016793 (2003).
- 239 23 Dudarev, S. L. The non-Arrhenius migration of interstitial defects in bcc
 240 transition metals. *Comptes Rendus Physique* **9**, 409-417,
 241 doi:10.1016/j.crhy.2007.09.019 (2008).
- 242 24 Swinburne, T. D., Dudarev, S. L., Fitzgerald, S. P., Gilbert, M. R. & Sutton,
 243 A. P. Theory and simulation of the diffusion of kinks on dislocations in bcc
 244 metals. *Physical Review B* **87**, 064108 (2013).
- 245 25 Arakawa, K., Amino, T. & Mori, H. One-dimensional glide motion of "naked"
 246 $1/2\langle 111 \rangle$ prismatic dislocation loops in iron. *ISIJ International* **54**, 2421-2424
 247 (2014).
- 248 26 Dausinger, F. & Schultz, H. Long-range migration of self-interstitial atoms in
 249 tungsten. *Physical Review Letters* **35**, 1773-1775 (1975).
- 250 27 Dausinger, V. F. Die Tieftemperaturerholung in elektronenbestrahltem
 251 Wolfram. *Philosophical Magazine A* **37**, 819-836,
 252 doi:10.1080/01418617808239211 (1978).
- 253 28 Mizubayashi, H. & Okuda, S. Elastic after-effect studies of self-interstitials in
 254 tungsten after fast neutron irradiation at 5 K. *Radiation Effects* **54**, 201-215,
 255 doi:10.1080/00337578108210049 (1981).
- 256 29 Dudarev, S. L., Derlet, P. M. & Woo, C. H. Driven mobility of self-interstitial
 257 defects under electron irradiation. *Nuclear Instruments and Methods in*
 258 *Physics Research Section B: Beam Interactions with Materials and Atoms*
 259 **256**, 253-259, doi:10.1016/j.nimb.2006.12.013 (2007).
- 260 30 Satoh, Y., Matsui, H. & Hamaoka, T. Effects of impurities on one-
 261 dimensional migration of interstitial clusters in iron under electron irradiation.
 262 *Physical Review B* **77**, 94135, doi:10.1103/PhysRevB.77.094135 (2008).
- 263 31 Ashcroft, N. W. & Mermin, N. D. *Solid State Physics*. (College Edition, New
 264 York, 1978).

265

266 Acknowledgements

267 This work was financially supported by JSPS KAKENHI (Grant No. 15H04244, and 18K18951),
 268 ImPACT Program of Council for Science, Technology and Innovation (Cabinet Office, Government of
 269 Japan), Q-LEAP Program (MEXT: Ministry of Education, Culture, Sports, Science and Technology -
 270 Japan), and the Iron and Steel Institute of Japan Research Promotion Grant. Part of this work was
 271 supported by the "Advanced Characterization Nanotechnology Platform, Nanotechnology Platform
 272 Programs" of MEXT, at Institute of Materials and Systems for Sustainability (Nanotechnology Open
 273 Facilities) in Nagoya University and at Research Centre for Ultra-High Voltage Electron Microscopy
 274 (Nanotechnology Open Facilities) in Osaka University, and TATARA Nanotechnology Project Centre

275 in Shimane University. M.C.M. acknowledges support from the GENCI -(CINES/CCRT) computer
276 centre under Grant No. A0050906973. A.M.G. and M.C.M acknowledges the financial support of the
277 Cross-Disciplinary Program on Numerical Simulation of CEA, the French Alternative Energies and
278 Atomic Energy Commission. S.P.F. acknowledges support from the UK EPSRC, grant number
279 EP/R005974/1. The work at CCFE has been carried out within the framework of the EUROfusion
280 Consortium and has received funding from the Euratom research and training programme 2019-2020
281 under grant agreement No 633053 and funding from the RCUK Energy Programme [grant number
282 EP/P012450/1]. The views and opinions expressed herein do not necessarily reflect those of the European
283 Commission.

284

285 **Author contributions**

286 K.A., M.C.M. and L.P. designed the study. K.A., T.Y., T.A., S.A., Y.Y., K.H., N.T., H.Y., T.Y. and H.M.
287 performed the experiments. M.C.M., S.P.F., L.P., D.N.M., A.M.G., S.L.D., P.W.M. and T.D.S.
288 performed the theoretical works. K.A., M.C.M., S.P.F., and S.L.D. wrote the main draft. All authors
289 discussed the results and commented on the manuscript.

290

291 **Additional information**

292 Supplementary information is available in the online version of the paper. Reprints and permissions
293 information is available online at www.nature.com/reprints. Correspondence and requests for materials
294 should be addressed to K.A.

295

296 **Competing financial interests**

297 The authors declare no competing financial interest.

298

299 **METHODS**

300 **Specimen preparation.** We cut (011) discs from one grain of an ingot of high-purity
301 coarse-grained polycrystalline tungsten (99.9999 mass % JX Nippon Mining & Metals
302 Co., Tokyo, Japan; impurity amounts of the ingot are given in Ref. [32]). The discs were
303 thinned to 0.1mm, using spark erosion and mechanical polishing, then perforated at the
304 centre by electropolishing so the periphery of the hole became cross-sectionally wedge-
305 shaped for TEM observations.

306

307 **Production of SIA clusters.** We used high-energy electron irradiation in a HVEM
308 (Hitachi H-3000) to create SIAs and vacancies in the thin foil specimens. The
309 acceleration voltage was 2000 kV, and a temperature of 105 K was maintained using a
310 liquid-nitrogen-cooled specimen holder (Oxford Instruments). We note that the thermal
311 migration of vacancies is frozen at temperatures below 620-900 K⁹. The beam flux was
312 $1 \times 10^{24} \text{ m}^{-2}\text{s}^{-1}$, and the dose was $4 \times 10^{25} \text{ m}^{-2}$.

313 During 2000-keV electron irradiation, pairs of SIAs and vacancies are produced³³ via
314 knock-on displacement. Based on our recent work^{19,32}, the point defect reactions
315 proceed as follows: most of the highly mobile 1D-moving SIAs react with vacancies,
316 or escape to the foil surface, where they are annihilated. Surviving SIAs bind to
317 impurity atoms and form embryonic SIA clusters, that grow by absorbing other SIAs,
318 and take the form of $\mathbf{b} = \frac{1}{2}\langle 111 \rangle$ dislocation loops. These clusters are intrinsically
319 highly mobile, yet they are trapped by impurities and remain stationary. Vacancies that
320 do not react with SIAs accumulate throughout the irradiated area of the specimen.

321 Using TEM, the average size and density of the SIA formed clusters under the above
322 condition were found to be approximately 3-4 nm and $4 \times 10^{22} \text{ m}^{-3}$, respectively.
323 Accumulated vacancies are not visible in the TEM. After the irradiation, the specimen
324 was aged at approximately 300 K. This allows the clusters trapped by weak impurity
325 atoms with shallow potential wells to thermally escape and move, leading to
326 coalescence with other clusters³⁴, escape to the specimen surfaces, or to trapping by
327 stronger impurities with deeper wells. However, even after aging for several months,
328 we did not see any significant change in the cluster density, demonstrating that thermal
329 escape of SIA clusters from the deeper wells hardly occurs even at 300 K.

330

331 **TEM observation of the 1D motion of SIA clusters in response to high-energy**

332 **electron irradiation.** We then used the electron beam to induce the vacancy mobility,
333 with acceleration voltages of 100, 150, 300, 500 (Hitachi H-9000UHV), 1000, and
334 2000kV (H-3000) – all except 2000kV are below the threshold for point defect
335 generation in tungsten³³. Additional very intense irradiations were carried out at
336 1000kV using a JEOL JEM 1000K RS. Beam fluxes ranged from 5×10^{22} to 2×10^{25}
337 $\text{m}^{-2}\text{s}^{-1}$, and temperatures ranged from 17-300 K (where no thermal migration of
338 vacancies takes place⁹). We achieved these temperatures using liquid-helium-cooled
339 specimen holders (Oxford Instruments), in which the temperature is measured with a
340 thermocouple attached to the specimen mount, so the measured temperature is the
341 average over the whole specimen.

342 The specimen thickness ranged from 50 to 70 nm (measured using equal-thickness
343 fringes³⁵). The observations were carried out using the weak-beam dark-field
344 technique³⁶ with a reflection of $\mathbf{g} = 200$. Under this condition, all SIA clusters in the
345 form of prismatic dislocation loops with a $\mathbf{b} = \frac{1}{2}\langle 111 \rangle$ type Burgers vector and a
346 diameter greater than approximately 2 nm were imaged. The dynamic response of the
347 clusters was monitored and recorded with CCDs having frame rates of 30 fps for H-
348 9000UHV and H-3000, and 15 fps for JEM 1000K RS.

349 We define the motion frequency of the clusters as the ratio of the number of cluster
350 hops observed per unit time divided by the number of observable clusters, i.e. the
351 average motion frequency of individual SIA clusters.

352

353 **Motion frequency and the ballistic and kinetic rates of SIA clusters.** Our
354 experiments measure the average motion frequency of SIA clusters under electron
355 irradiation as simultaneously observed in the transmission electron microscopes. The
356 average motion frequency at irradiation (observation) time t is defined as $\nu_{\text{MF}}(t) =$
357 $n_{\text{m}}/(n \Delta t)$: the ratio of the number of clusters that move (n_{m}) divided by the total
358 number of observed clusters (n) in the observation duration Δt .

359 The measured rates ν_{MF} are the combined results of motion induced by directly by the
360 irradiation, and stochastic motion induced by the underlying phonon bath.
361 Consequently, the motion frequency is impacted by irradiation conditions, in particular
362 the electron beam flux Φ and energy E . The temperature T also influences the
363 experimental observations through the phonon bath, meaning that the motion frequency
364 is a function defined on a 4 dimensional space $\nu_{\text{MF}}(t, T, \Phi, E)$. [Figure 3](#) illustrates the
365 temperature dependence, and [Fig. 2d-g](#) shows the behaviour of the motion frequency

366 with respect to the other variables. Here we derive an expression for the motion
 367 frequency in the context of the experiments.

368 Detailed experimental analysis suggests that the shrinkage of the clusters (Fig. 2a)
 369 originates from irradiation-induced vacancy motion (Fig. 2b). Since the impurities are
 370 immobile, the erosion of the clusters by the vacancies increases the distance between
 371 them and the impurities, which leads to the de-trapping of the clusters from the
 372 impurities. We call this mechanism of the cluster de-trapping by this process the
 373 *indirect de-trapping mechanism*. Since it depends on the radiation-mobilized vacancies
 374 eroding the SIA clusters, the cluster motion frequency is proportional to the vacancy
 375 concentration, c_V . These vacancies are absorbed by the clusters, and other sinks such
 376 as the specimen surface, at a rate proportional to the concentration of vacancies itself:
 377 $\dot{c}_V \propto -c_V$. As long as no new Frenkel pairs are created, this leads to an exponential
 378 decay of vacancy concentration as a function of time, and the corresponding variation
 379 of the cluster motion frequency. This is precisely what we find in Fig. 2cd, in the limit
 380 of short observation time.

381 In the indirect mechanism, cluster de-trapping is also impacted by the thermal rate at
 382 which the clusters escape from the impurities. At a given cluster-impurity separation,
 383 d_k , sufficiently large that the trapping energy is low, the thermal escape rate Γ_{th}^k is
 384 governed by the cluster-impurity trapping energy ΔV_{trap}^k for that distance (see next
 385 section). If we have n_k cluster-impurity sets at given cluster-impurity separation d_k ,
 386 then the number of clusters that jump within the observation time is $a c_V n_k \Gamma_{th}^k \Delta t$.
 387 Prefactor a accounts for the effect of the beam flux and energy on the observations.

388 Since the incident electron energy is high, what we call the *direct de-trapping*
 389 *mechanism* – direct collision of the electron with a cluster itself²⁹ or the impurity that
 390 traps the cluster³⁰ – can also release the cluster. The de-trapping rate Γ_d associated with
 391 this direct mechanism is independent of temperature and uniform in time, depending
 392 only on the concentration of cluster-trapping impurities and the flux and energy of the
 393 electrons. The probability of releasing a cluster from an impurity via the direct
 394 mechanism is $n \Gamma_d \Delta t$.

395 Consequently, the measured motion frequency can be written as

$$396 \quad \nu_{MF} = \frac{n_{indirect} + n_{direct}}{n \Delta t} = \frac{\sum_k a c_V n_k \Gamma_{th}^k(T) \Delta t + n \Gamma_d \Delta t}{n \Delta t}$$

397 Or, in a simpler form, if we assume that in the system the initial vacancy density $c_V(0)$
 398 decreases in time with a decay factor α_v :

399
$$\nu_{\text{MF}} \sim \sum_k a c_v(0) e^{-\alpha_v t} \frac{\Gamma_{\text{th}}^k(T) n_k}{n} + \Gamma_d = e^{-\alpha_v t} \left[\sum_k a c_v(0) \frac{\Gamma_{\text{th}}^k(T) n_k}{n} \right] + \Gamma_d$$

400 This theoretical expression for the motion frequency is fully compatible with all the
401 experimental evidence described in the body of the paper and illustrated in Fig. 2.

402 Firstly, the experimental observations shown in Fig. 2de indicate that the motion
403 frequency decreases exponentially in time, and after several hundred seconds, the
404 frequency's exponential decay becomes a constant plateau. This reflects the local
405 exhaustion of vacancies near the clusters, and the transition to de-trapping by direct
406 electron impacts, through what we term the direct mechanism. The $t \rightarrow \infty$ limit
407 corresponds to the frequency of de-trapping events associated with the direct
408 mechanism $\nu_{\text{MF}} \rightarrow \Gamma_d$. On the other hand, in the limit of $t \rightarrow 0$:

409
$$\nu_{\text{MF}}(t \rightarrow 0) = \left[\sum_k a_k c_v(0) \frac{\Gamma_{\text{th}}^k(T) n_k}{n} \right] + \Gamma_d \sim \text{const} \times \Gamma_{\text{th}}^0(T) + \Gamma_d,$$

410 we have access, up to multiplicative (const) and additive (Γ_d) constants, to the dominant
411 thermal/quantum rate $\Gamma_{\text{th}}^0(T)$ on the nature of which, classical or quantum, our study is
412 focused. We note that the higher the beam energy, the greater is the part played by the
413 direct mechanism of de-trapping, and the sooner the hopping rate reaches the
414 asymptotic value. The plateaus are also higher for higher beam energies, reflecting the
415 direct mechanism's expected variation as a function of the incident electron beam
416 energy.

417 Secondly, Fig. 2f shows the cluster motion frequency's strong dependence on the beam
418 intensity at 300 kV, clearly illustrating a role the irradiation contributes through the
419 multiplicative constants. Note that no further Frenkel pairs are created if the beam
420 energy is at or below 1000 kV.

421 Finally, Fig. 2g shows the electron energy dependence of $\nu_{\text{MF}}(t \rightarrow 0, E)$, together with
422 the athermal radiation-driven vacancy migration rate under the beam Γ_{vac} . The Γ_{vac}
423 value is proportional to the product of beam flux and the cross section for radiation
424 induced vacancy migration³⁷,

428
$$\sigma_{\text{mig}} \approx \int_{E_{\text{mig}}^V}^{E_{\text{K, max}}} \frac{E_{\text{K}}}{E_{\text{mig}}^V} \frac{d\sigma}{dE_{\text{K}}} dE_{\text{K}},$$

425 where E_{K} is the kinetic energy transferred from an incident electron to a tungsten atom
426 neighbouring a vacancy, E_{mig}^V is the vacancy migration energy (1.78 eV³⁸), and $d\sigma$ is
427 the differential cross section for the electron-tungsten atom collision calculated using

429 the McKinley-Feshbach formula³⁹. The high degree of correlation between the two is
430 abundantly clear, providing a further confirmation of the vacancy origin of the indirect
431 mechanism of cluster de-trapping and migration.

432 A natural question is whether this approach has sufficient accuracy to reveal the
433 classical or quantum nature of the cluster migration rate. The quantity of interest is the
434 logarithm of the motion frequency, which can be written as:

$$435 \quad \ln v_{\text{MF}}(t \rightarrow 0) = \ln[\Gamma_{\text{th}}^0(T) + \Gamma_{\text{d}}] \sim \ln \Gamma_{\text{th}}^0(T) + \frac{\Gamma_{\text{d}}}{\Gamma_{\text{th}}^0(T)}$$

436 The second term of the right side is easily estimated from the ratio of asymptotic limits
437 $v_{\text{MF}}(t \rightarrow 0)/v_{\text{MF}}(t \rightarrow \infty)$. This quantity is in the order of 10^{-1} and 10^{-2} at 1000 keV
438 and 500 keV, respectively, for 289-298 K (Fig. 2d). Also, it is shown to be no higher
439 than 0.2 at 300 keV even at 31 K (Fig. ED4). This analysis shows that in terms of
440 observed logarithm of $v_{\text{MF}}(t \rightarrow 0)$, the effect of direct de-trapping mechanism is visible
441 at the level after the first or even the second place after the decimal point. Hence, the
442 direct and indirect contributions to the motion frequency can be reliably separated.

443 We provide the details of the statistical procedure used for measuring v_{MF} . One
444 specimen involved 1×10^2 areas for 2000-keV electron irradiation for the SIA cluster
445 production, at maximum. The n value within one area of interest (AOI) centred at a
446 2000-keV electron irradiated area was $(1 - 2) \times 10^2$ for $t = 0$ s. This n value was the
447 practical upper limit under the lowest TEM magnification enabling the observation of
448 the cluster motion. In the time dependence of $v_{\text{MF}}(t)$ (Figs. 2de and ED4), matching
449 symbols correspond to the same AOI, and in the beam flux dependence of
450 $v_{\text{MF}}(t \rightarrow 0, \Phi)$ (Fig. 2f), energy dependence of $v_{\text{MF}}(t \rightarrow 0, E)$ (Fig. 2g), and
451 temperature dependence of $v_{\text{MF}}(t \rightarrow 0, T)$ (Fig. 3), individual data points correspond
452 to different AOIs. The error in the v_{MF} value was evaluated under the assumption that
453 both the distributions of n and n_{m} for a given AOI independently obey the Poisson
454 statistics. Then, the error in a measured v_{MF} value becomes $v_{\text{MF}} \sqrt{\frac{1}{n} + \frac{1}{n_{\text{m}}}}$. The data sets
455 for temperature dependence of $v_{\text{MF}}(t \rightarrow 0, T)$ under the fixed other conditions (Fig. 3)
456 were acquired from the areas belonging to an identical TEM specimen so that the
457 impurity concentration in the measured areas was very similar level.

458

459 **Diffusion rates in quantum and classical phonon baths.** The archetypal problem of
460 a particle traversing a potential barrier has been treated exhaustively; see Ref. [40] for a

461 thorough review. For a barrier height $\Delta V \gg k_B T$, the classical escape rate is given by
 462 the Arrhenius function $\Gamma_{\text{th}}^{\text{cl}} = f_{\text{cl}} \exp(-\Delta V/k_B T)$, where the classical prefactor f_{cl} can
 463 be loosely interpreted as an attempt frequency. As $k_B T$ rises towards ΔV the Arrhenius
 464 function breaks down, and the rate transitions to a form linear in the temperature^{11,23}
 465 (manifested as a sharp steepening on an Arrhenius plot). For barriers $\Delta V \sim k_B T$ or less,
 466 the particle migrates stochastically, being slowed only by the dissipative coupling
 467 between the particle and the underlying phonon bath. This is quantified by the friction
 468 parameter γ , and the rate is proportional to $k_B T/\gamma$ ^{11,23,41}. If $\Delta V \ll k_B T$, the friction can
 469 be absorbed into f_{cl} ^{40,42}. Both standard rate formulae originate from the classical
 470 Boltzmann distribution for the phonons. For clusters escaping from traps, the barrier to
 471 be overcome is $\Delta V = \Delta V_{\text{p}} + \Delta V_{\text{trap}}$, the sum of the Peierls barrier and the critical
 472 binding energy of the impurity or vacancy respectively. Therefore the diffusion rate is
 473 the product of two independent probabilities: the probability related to the free
 474 migration of the SIA cluster through the Peierls potential in the absence of a trap, and
 475 the escape probability from the trap itself: $\Gamma_{\text{th}}^{\text{cl}}(T) = \Gamma_{\text{p}}(T) \times \Gamma_{\text{trap}}(T)$. $\Delta V_{\text{trap}} \gg k_B T$,
 476 so Γ_{trap} is Arrhenius in the classical limit. Since the Peierls barrier ΔV_{p} for SIA clusters
 477 (a.k.a. $\frac{1}{2}\langle 111 \rangle$ loops) is small, i.e. of order $k_B T$, the total classical rate becomes:

$$478 \quad \Gamma_{\text{th}}^{\text{cl}}(T) = \text{const.} \times k_B T \times \exp\left(-\frac{\Delta V_{\text{trap}}}{k_B T}\right) \quad (1)$$

479 We note that the constant prefactor above can take on a weak temperature dependence
 480 in other formulations of the rate; we obtain similar fits in either case and our conclusions
 481 are unaffected.

482 The full quantum-mechanical development is more complicated. Here, the Boltzmann
 483 distribution is replaced by either the Bose-Einstein (BE) or Fermi-Dirac distribution,
 484 for bosons or fermions respectively. For tungsten or impurity atoms the ground state
 485 has integer spin and hence obeys Bose-Einstein statistic. A simple way to recover the
 486 BE phonon distribution whilst retaining the form of the classical rate formulae is to
 487 renormalize the temperature to mimic the true quantum statistics^{15,42,43}. Consider a
 488 crystal with periodic boundary conditions represented by N atoms in a box. Imposing
 489 equality of the classical and quantum energies, the (renormalized, effective) classical
 490 temperature and the (true) quantum temperature should be related by the relation:

$$491 \quad (3N - 3)k_B T_c = \int d\omega \hbar\omega \left(\rho_{\text{BE}}(\omega, T_q) + \frac{1}{2} \right) n(\omega)$$

492 where T_c and T_q are the (renormalized, effective) classical and (true) quantum
 493 temperatures respectively. $n(\omega)$ is the density of states of the phonon gas, normalized

494 to the number of modes, and $\rho_{BE}(\omega, T)$ is the BE distribution function. Therefore, the
 495 effective classical temperature is a function of the true quantum temperature $T_c =$
 496 $f(T_q)$.

497 For temperatures higher than the Debye temperature T_D , $\hbar\omega \ll k_B T$, the energy of one
 498 oscillator becomes:

$$499 \quad \hbar\omega \left(\rho_{BE}(\omega, T_q) + \frac{1}{2} \right) \approx \frac{\hbar\omega}{2} + k_B T_q \left(1 - \frac{\hbar\omega}{2k_B T_q} + K \right) = k_B T_q,$$

500 and the classical and quantum temperatures are very close. When the (true) quantum
 501 temperature T_q tends to zero K, the effective classical temperature T_c tends to a finite
 502 limit, capturing the zero point energy:

$$503 \quad (3N - 3)k_B T_c = \int d\omega \frac{1}{2} \hbar\omega n(\omega)$$

504 The simple form $T_c = \sqrt{\tau_c^2 + T_q^2}$ satisfies these limits (see [Fig. ED5](#)). Therefore, the
 505 quantum rates can be estimated by simply renormalizing the temperature in [equation](#)
 506 [\(1\)](#) yielding:

$$507 \quad \Gamma_{th}^{QM}(T) = \text{const.} \times k_B \sqrt{\tau_c^2 + T^2} \times \exp \left(- \frac{\Delta V_{\text{trap}}}{k_B \sqrt{\tau_c^2 + T^2}} \right) \quad (2)$$

508 We also attempted to fit the data with up to three distinct classical barrier escape
 509 mechanisms operating simultaneously. Only the quantum rates explain the observed
 510 temperature dependence.

511 **Quantum TST rates.** For deep tunneling, we computed the rate by numerically
 512 integrating the quantum transition state theory rate expression⁴²

$$513 \quad \Gamma_{th}^{QTST} = (hZ_0)^{-1} \int W(E) e^{-E/k_B T} dE,$$

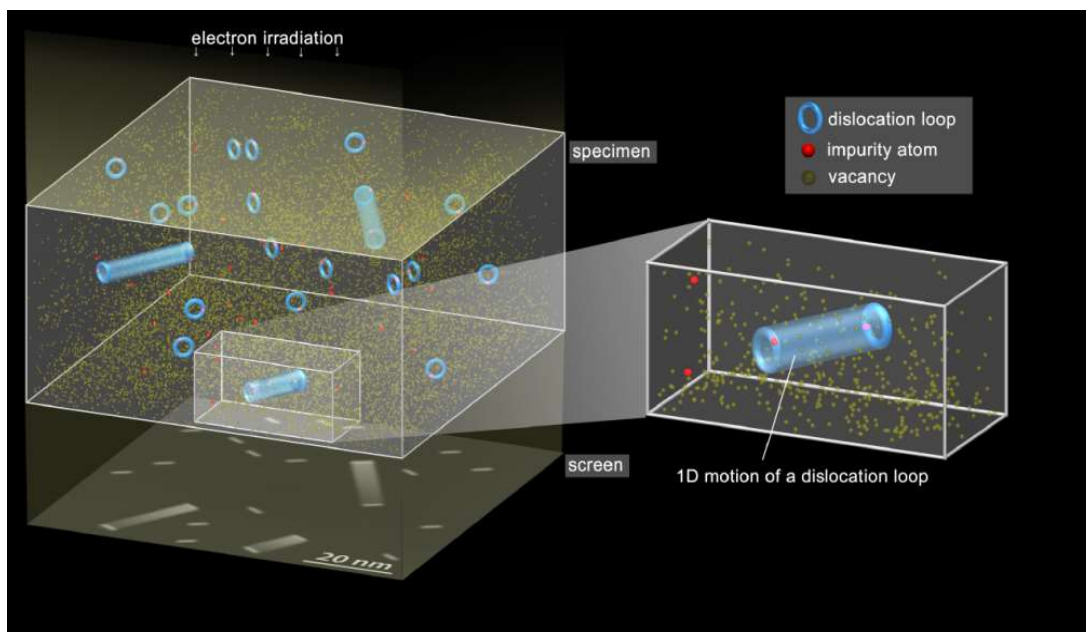
514 where h is the Planck constant and $W(E)$ is the transfer integral at energy E for the sech-
 515 squared impurity interaction potential predicted by the Frenkel Kontorova model, (see
 516 [Supplementary Discussion 1](#)). The data can be fitted with a barrier height of 55 meV,
 517 but requires an unrealistically low effective cluster mass of $m_W/200$ (m_W is the mass
 518 of one tungsten atom). The remaining parameters (potential width and curvature) are
 519 fixed by the Arrhenius limit, which applies to the highest temperature points in the
 520 dataset.

522 **References**

- 523 32 Amino, T., Arakawa, K. & Mori, H. Activation energy for long-range
524 migration of self-interstitial atoms in tungsten obtained by direct measurement
525 of radiation-induced point-defect clusters. *Philosophical Magazine Letters* **91**,
526 86-96, doi:10.1080/09500839.2010.533133 (2011).
- 527 33 Maury, F., Biget, M., Vajda, P., Lucasson, A. & Lucasson, P. Frenkel pair
528 creation and stage I recovery in W crystals irradiated near threshold. *Radiation*
529 *Effects* **38**, 53-65, doi:10.1080/00337577808233209 (1978).
- 530 34 Arakawa, K., Amino, T. & Mori, H. Direct observation of the coalescence
531 process between nanoscale dislocation loops with different Burgers vectors.
532 *Acta Mater* **59**, 141-145, doi:10.1016/j.actamat.2010.09.018 (2011).
- 533 35 Hirsch, P. B., Howie, A., Nicholson, R. B., Pashley, D. W. & Whelan, M. J.
534 *Electron Microscopy of Thin Crystals*. (Butterworths, London, 1965).
- 535 36 Jenkins, M. L. & Kirk, M. A. *Characterization of Radiation Damage by*
536 *Transmission Electron Microscopy*. (Institute of Physics, Bristol and
537 Philadelphia, 2001).
- 538 37 Kiritani, M. Electron Radiation Induced Diffusion of Point Defects in Metals.
539 *Journal of the Physical Society of Japan* **40**, 1035-1042,
540 doi:10.1143/JPSJ.40.1035 (1976).
- 541 38 Nguyen-Manh, D., Horsfield, A. P. & Dudarev, S. L. Self-interstitial atom
542 defects in bcc transition metals: Group-specific trends. *Physical Review B* **73**,
543 020101 (R) (2006).
- 544 39 Oen, O. S. Cross sections for atomic displacements in solids by fast electrons.
545 (1965).
- 546 40 Hänggi, P., Talkner, P. & Borkovec, M. Reaction-rate theory: fifty years after
547 Kramers. *Reviews of Modern Physics* **62**, 251-341 (1990).
- 548 41 Dudarev, S. L. Coherent motion of interstitial defects in a crystalline material.
549 *Philos Mag* **83**, 3577-3597, doi:10.1080/14786430310001599388 (2003).
- 550 42 Benderskii, V., Makarov, D. & Wight, C. *Chemical Dynamics at Low*
551 *Temperature*. (Wiley-Interscience, 1994).
- 552 43 Wang, C. Z., Chan, C. T. & Ho, K. M. Tight-binding molecular-dynamics
553 study of phonon anharmonic effects in silicon and diamond. *Physical Review*
554 *B* **42**, 11276-11283 (1990).
555

556 **Figures**

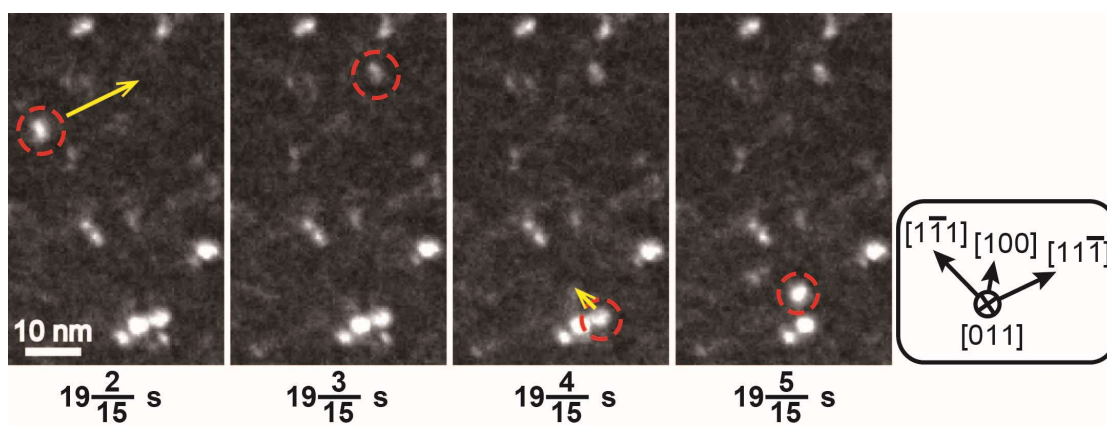
557 **a**



558

559

560 **b**

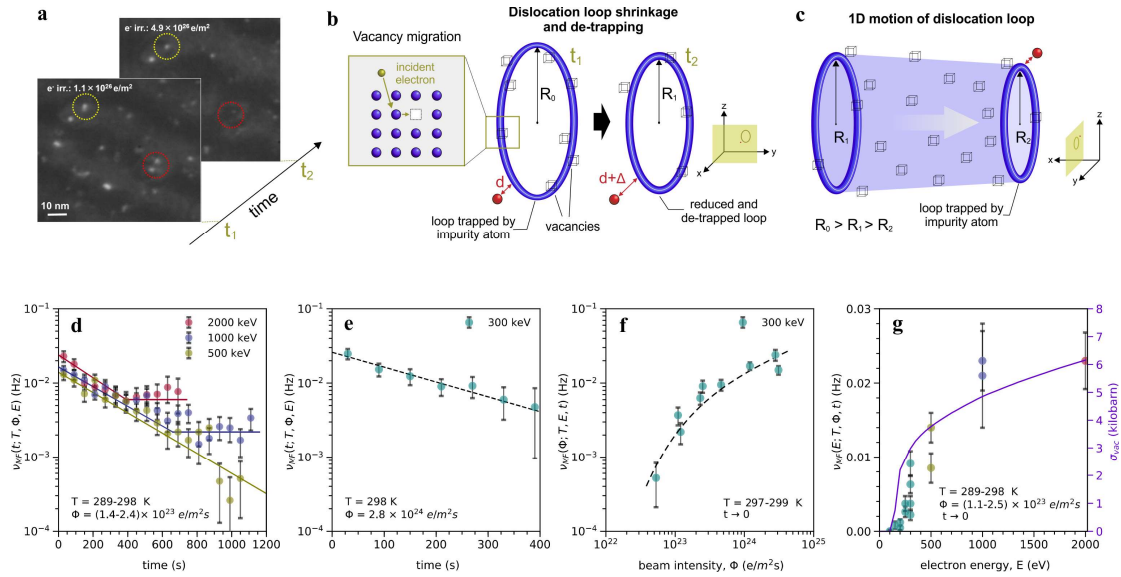


561

562 **Figure 1 | 1D SIA cluster motion.** **a:** Experimental setup. In a high-purity tungsten
 563 specimen, SIA clusters in the form of nanoscale $\frac{1}{2}\langle 111 \rangle$ dislocation loops are trapped
 564 by impurity atoms at their boundary. **b:** High-energy electron irradiation enables
 565 clusters to escape, and subsequently undergo fast 1D glide diffusion before being
 566 trapped by other impurity atoms. This 1D motion was monitored simultaneously
 567 (acceleration voltage: 1000 kV; beam intensity: $2 \times 10^{25} \text{ m}^{-2}\text{s}^{-1}$; temperature: 260 K, see
 568 [Supplementary Video 1](#)). Circled clusters move in the directions indicated by arrows,

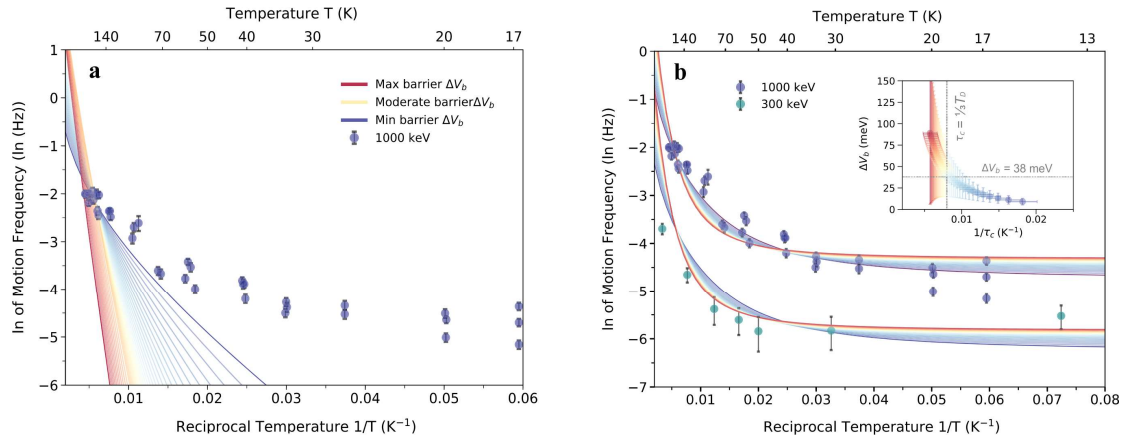
569 parallel to the $\langle 111 \rangle$ -type cluster Burgers vectors. The clusters hop distances of several
570 nm to a few tens of nm within a single 1/15 s movie frame.

571



572

573 **Figure 2 | Characterization of the motion frequency of SIA cluster de-trapping. a:**
 574 SIA cluster (dislocation loop) shrinking under the beam (acceleration voltage: 300 kV;
 575 beam intensity: $3.1 \times 10^{24} \text{ m}^{-2}\text{s}^{-1}$; temperature: 299 K). Vacancies in tungsten are
 576 thermally immobile at 299 K, and so the only way the SIA clusters can shrink is via the
 577 absorption of radiation-mobilized vacancies. **b:** The clusters escape by increasing the
 578 distance between their perimeter and the impurity, from d to $d + \Delta$, as they shrink from
 579 radius R_0 at time $t_1 \rightarrow R_1 < R_0$ at time t_2 . This reduces the binding energy (see
 580 [Supplementary Discussion 1](#)) **c:** Stop-and-go motion of the loop in the clouds of
 581 vacancies and impurities. Once the loop has escaped from the impurity, it migrates until
 582 is trapped by another impurity. During this macro-jump, over many Peierls barriers, the
 583 loop sweeps through the surrounding vacancy clouds, decreasing its effective radius to
 584 $R_2 < R_1$. **d, e:** Motion frequency decaying exponentially with time under irradiation
 585 which corresponds to indirect mechanism (see [Methods](#)). Plateaus are reached when
 586 the supply of vacancies local to the clusters is exhausted by annihilation, and the direct
 587 mechanism takes over (see [Methods](#)). **f:** Motion frequency increasing with beam
 588 intensity (time: 0 – 60 s). **g:** Motion frequency vs. beam energy and cross section for
 589 radiation-induced vacancy migration (time: 0 – 60 s) (see [Methods](#)).



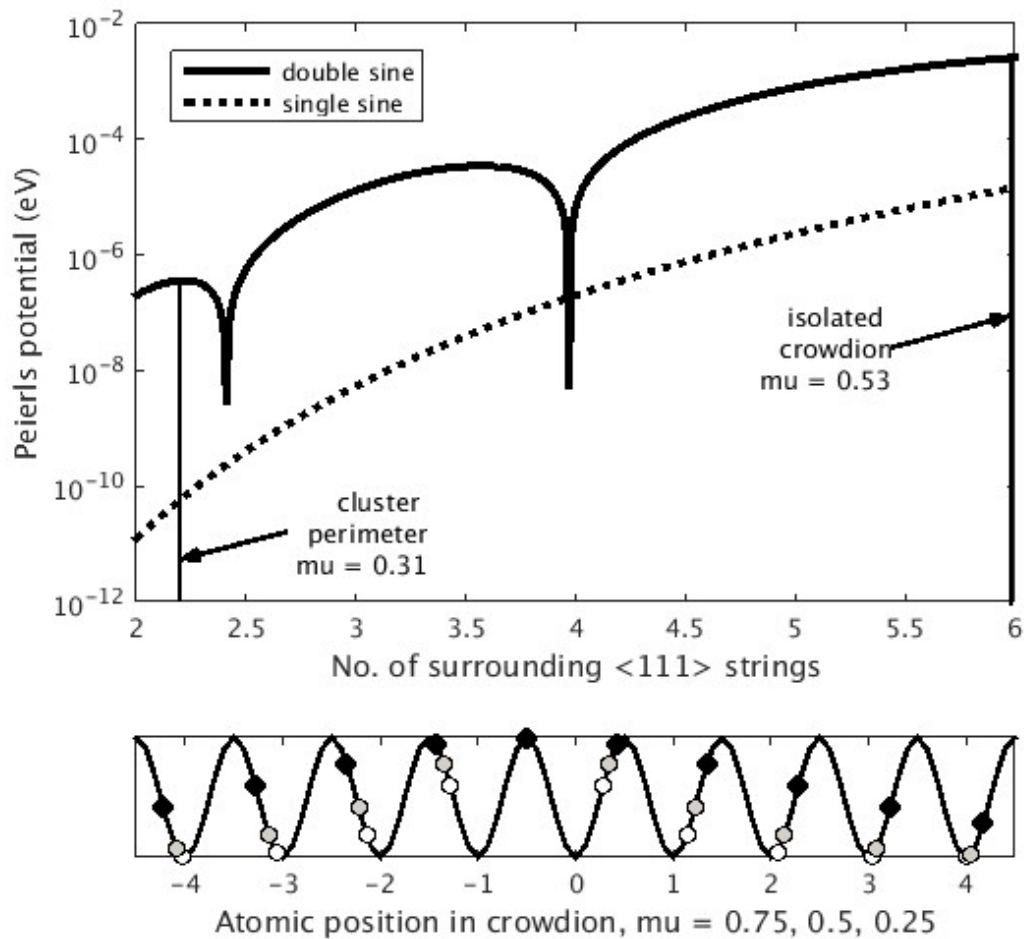
590

591 **Figure 3 | Motion frequency of SIA cluster de-trapping vs. temperature.** Data
 592 points show measured motion frequency vs. temperature (data taken in first 60 s of
 593 irradiation. Blue points: beam energy 1000 keV, beam intensity $2 \times 10^{25} \text{ m}^{-2}\text{s}^{-1}$; green
 594 points: beam energy 300 keV, beam intensity $(2 - 4) \times 10^{24} \text{ m}^{-2}\text{s}^{-1}$). Some error bars are
 595 too small to be visible. **a:** All possible classical fits of one single dataset, at beam energy
 596 of 1000 keV, for activation barriers between 10 meV (blue) and 90 meV (red). Thin
 597 lines between are intermediate values. No classical fit can capture the temperature
 598 dependence. **b:** As panel **a** but using quantum mechanical rate function. Both 1000 and
 599 300 keV datasets were fitted simultaneously, with a single parameter to account for the
 600 ratio of the two (we obtained a value of 4.52 for the ratio, consistent with Fig. 2g, see
 601 [Methods](#)). Inset: fitted correlation between activation barrier and critical temperature
 602 τ_c (see text and [Methods](#)), with corresponding error bars. The value of the effective
 603 activation barrier at $\tau_c = \frac{1}{3} T_D$ (T_D : Debye temperature) is 38 meV.

604

605 **Extended Display Items**

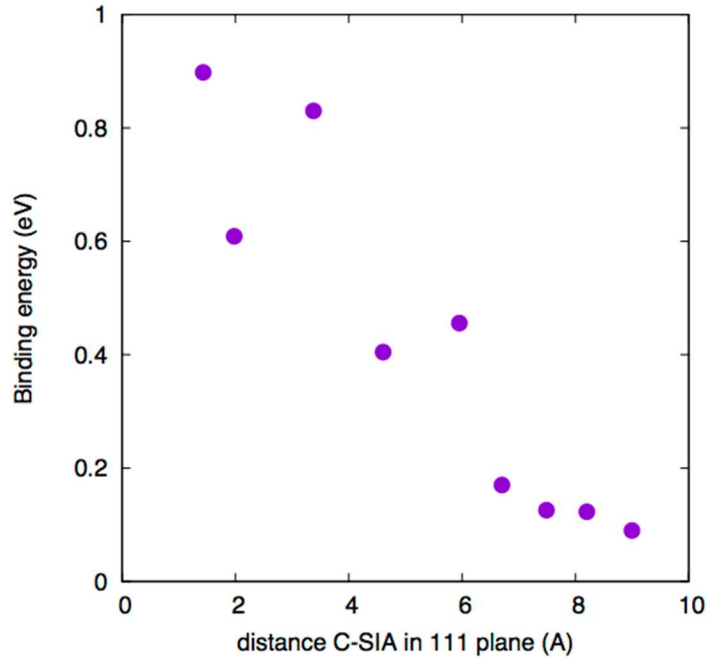
606



607

608 **Figure ED1** | Top: suppression of Peierls potential as delocalization increases (and μ
609 decreases). Both the standard single-sine and more accurate double-sine Frenkel-
610 Kontorova models predict a negligibly small barrier for cluster diffusion after escape
611 from the traps. Bottom: atomic positions showing increased delocalization as μ
612 decreases from 0.75 (open circles) through 0.5 (grey circles) to 0.25 (solid circles).

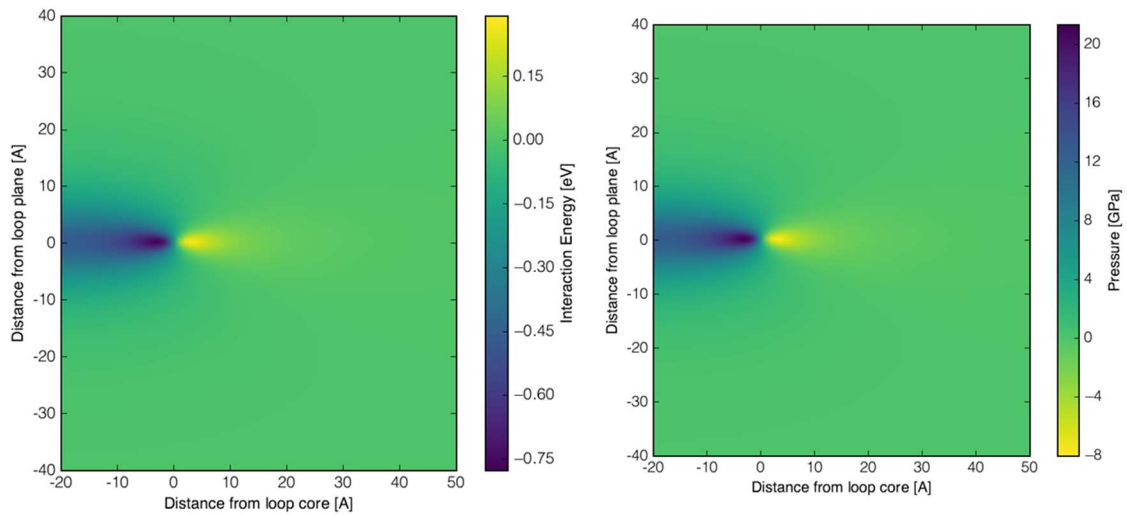
613



614

615 **Figure ED2a** | DFT calculation of the SIA-carbon binding energy vs. separation in
 616 plane transverse to the crowdion axis.

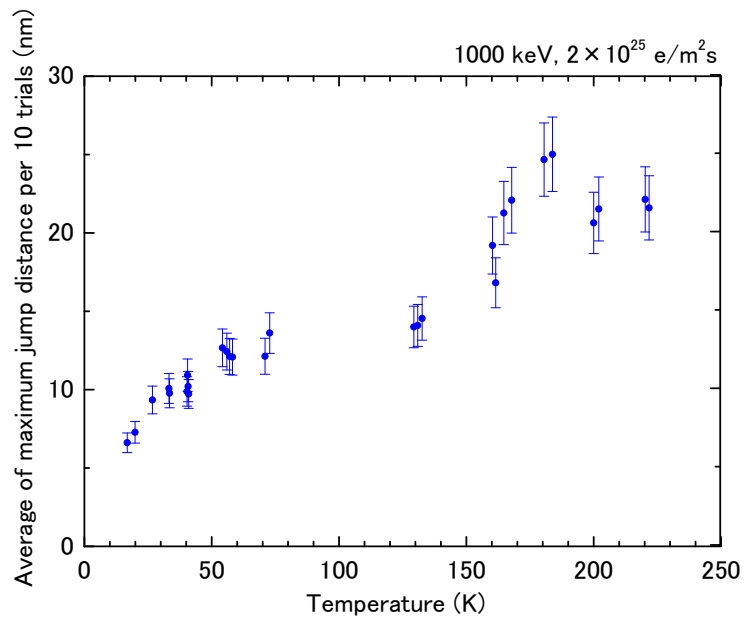
617



618

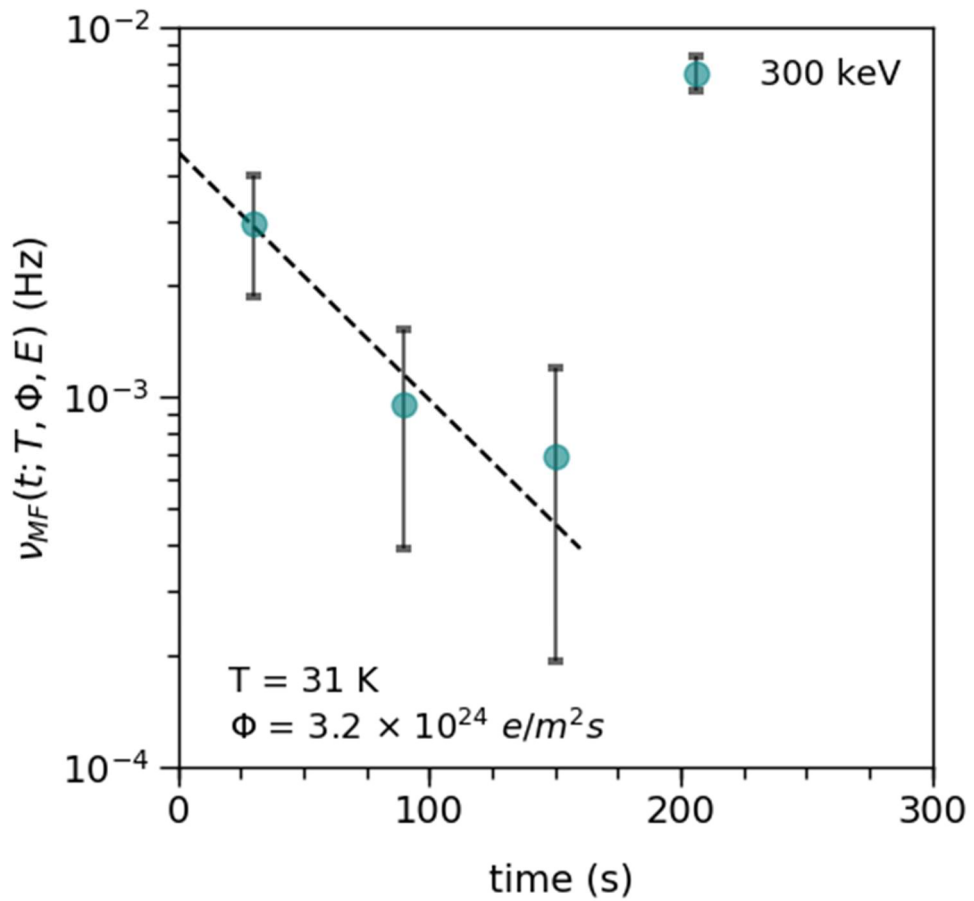
619 **Figure ED2b** | Elastic calculation of the SIA cluster-dilatation centre binding energy
 620 (left) and cluster pressure field (right).

621



622

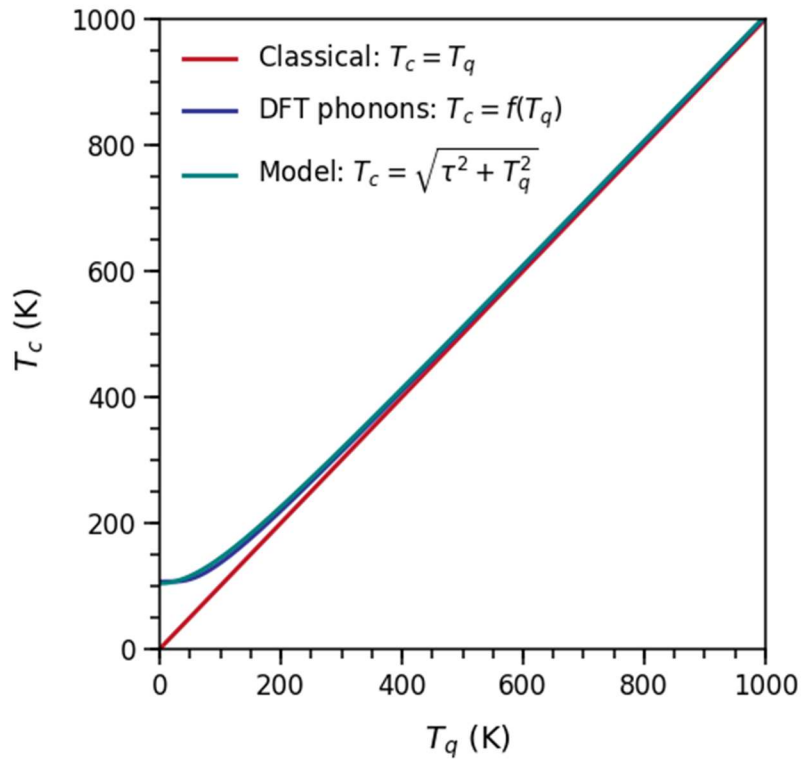
623 **Figure ED3** | Average maximum hop distance per 10 hops vs temperature. A range of
 624 binding energies exist, corresponding to different cluster-impurity separations. This
 625 means more impurities are effective traps at lower temperatures, leading to a reduced
 626 hop distance.



627

628 **Figure ED4** | Motion frequency vs irradiation time at 31 K, with beam energy 300 keV.
 629 The decrease in motion frequency, attributed to the depletion of vacancies near the
 630 clusters, is still clear, and demonstrates that the direct mechanism (which would induce
 631 a motion frequency constant in time) is not wholly responsible for the cluster motion.
 632 Indeed, at short times the motion is dominated by the indirect mechanism, by at least a
 633 factor of 5.

634



635

636 **Figure ED5** | The correspondence between the effective classical temperature T_c (our
 637 model) and the quantum (true) temperature T_q of perfect bulk bcc W. The classical,
 638 DFT phonons and our model are shown in red, dark blue and light blue respectively.